Structure and phases of the Au(001) surface: Absolute x-ray reflectivity

B. M. Ocko, Doon Gibbs, and K. G. Huang
Department of Physics, Brookhaven National Laboratory, Upton, New York 11973

D. M. Zehner
Solid State Division, Oak Ridge National Laboratory, Oak Ridge, Tennessee 37831

S. G. J. Mochrie
Center for Materials Science and Engineering and Department of Physics, Massachusetts Institute of Technology, Cambridge, Massachusetts 02139
(Received 6 November 1990; revised manuscript received 24 May 1991)

Specular and nonspecular absolute x-ray-reflectivity measurements have been performed on the Au(001) surface between $T=300$ and 1250 K. At all temperatures the surface-normal vibrational amplitudes are increased above the corresponding bulk thermal vibrational amplitude (Debye-Waller factor). Below $T=1170$ K, the surface is well described by an incommensurate, corrugated, hexagonal overlayer. The corrugation propagates several layers into the bulk. Above $T=1170$ K there is an abrupt decrease in the specular and nonspecular reflectivities, which we interpret in terms of surface disordering.

I. INTRODUCTION

Despite the planes of square symmetry lying immediately beneath, the Au(001) surface exhibits a room-temperature reconstruction in which the top layer forms a distorted-hexagonal monolayer. In this and a previous paper,[1] we present the results of a comprehensive x-ray-diffraction study of this surface between room temperature and close to the bulk triple point ($T_t=1337$ K). The results presented in Ref. 1 demonstrate that below $T=1170$ K the structure is hexagonal and incommensurate with the bulk substrate. The existence of satellite peaks spaced at intervals equal to the wave-vector difference between hexagonal and substrate periodicities, however, suggests that these lattices are modulated (and lead to our designation of this phase as "distorted-hexagonal"). In addition, for temperatures less than $T=970$ K, there exist domains of the hexagonal overlayer which are rotated by $\pm 0.81°$ away from the cubic [110] direction (in coexistence with the aligned domains). At $T=970$ K, there is a reversible, rotational transformation at which the rotated domains become aligned. Finally, at $T=1170$ K there is a disordering transition, at which temperature all scattering associated with the hexagonal reconstruction disappears. In Fig. 1, the observed in-plane (H-K plane) diffraction patterns are shown for the three phases of the Au(001) surface.

In this paper, we give a complete account of measurements of the absolute x-ray reflectivity for the Au(001) surface. We refer to reflectivity as the coherent scattering along the surface-normal direction through the allowed in-plane wave vectors.[1-3] Specifically, specular reflectivity corresponds to the rod of scattering through the origin of Fig. 1, while nonspecular reflectivity corresponds to the rods through all other, in-plane wave vectors. For the present experiments, involving a reconstructed surface layer, we further classify the nonspecular reflectivity into the overlayer reflectivity, which corresponds to the reflectivity through in-plane hexagonal wave vectors, and the substrate reflectivity, which corresponds to the reflectivity through the bulk-allowed in-plane wave vectors. In the literature, the substrate reflectivity is called a truncation rod.[4] It is important to

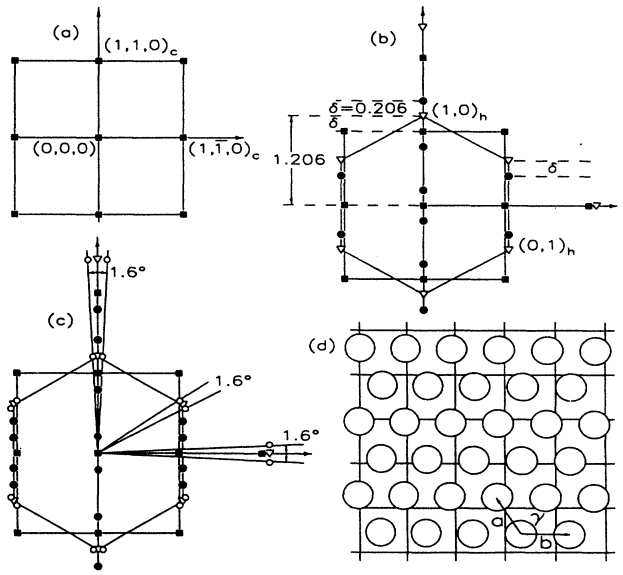

FIG. 1. In-plane diffraction pattern for the Au(001) surface. (a) disordered phase ($T>1170$ K); (b) distorted-hexagonal phase ($970K<T<1140$ K); (c) rotated, distorted-hexagonal phase ($T<970$ K). Each point represents a rod of scattering normal to the surface. (d) Real-space schematic view of a rotated domain. The square symbols represent the in-plane reflections from the underlying square symmetry of the (001) face and persist above the hexagonal disordering transition at 1170 K. Only one of the two symmetry equivalent domains is represented.

note that, in the present work, the specular and nonspecular reflectivities of the Au(001) surface have been obtained on an absolute scale. This imposes stringent constraints on subsequent modeling, and leads to a detailed three-dimensional characterization of the surface and near-surface structure, including the determination of the enhanced surface vibrational amplitudes, of the relaxations of the interplanar spacing at the surface, and of the corrugation amplitudes.

Briefly, for temperatures above $T=1170$ K, we find that the measured Q_z dependence (Q_z denotes the normal wave-vector transfer) of the reflectivity is consistent with a thin disordered surface film a few layers thick[5–12] and not with an ideally terminated crystal. In contrast, in the distored-hexagonal phase below $T=1170$ K, we have found that the top layer supports an incommensurate corrugation which propagates approximately five layers into the bulk. In addition, the interplanar spacing between the top and second layers is increased by 20%. At all temperatures, the thermal vibrational amplitudes (Debye-Waller factors) within the surface and near-surface layers are enhanced relative to their bulk values. Besides presenting our experimental results for the structure of the Au(001) surface, another purpose of this paper is to illustrate the dependence of the reflectivity on the layer-dependent crystalline order parameters $\rho_{\mathbf{G}}(n)$.[7–8,13,14] By definition, $\rho_{\mathbf{G}}(n)$ is the Fourier component of the electron density of the nth layer with in-plane wave vector $\mathbf{G}$. The variation of the nonspecular reflectivity with Q_z may be directly related to the real-space decay of $\rho_{\mathbf{G}}(n)$ in the neighborhood of the surface. A summary of these results and those of Ref. 1 has appeared previously.[13]

Before presenting the results of our x-ray-scattering measurements, we summarize the highlights of some recent discussions of surface disordering. Surface-induced disorder is plausibly a key to understanding bulk melting. For example, a liquid overlayer provides a nucleation site for bulk melting, which may explain the absence of superheating at the triple point.[15] Recent interest in surface melting has been rekindled in papers by Lipowsky and Speth.[16,17] Within mean-field theory, these authors considered a semi-infinite system described by a scalar order parameter and a free-energy functional which ordinarily gives rise to a discontinuous, first-order phase transition. However, even in the simplest case, that in which the interatomic coupling strength of surface atoms differs from that of bulk atoms by a constant, they discovered an elaborate phase diagram,[17] and predicted the possibility that a melted surface region may exist below the bulk ordering transition. The decay of the layer-dependent crystalline order parameter was calculated using a Landau theory of surface melting.[7,8,14] In this case $\rho_{\mathbf{G}}(n)$ was found to decay as a function of n over a $\mathbf{G}$-dependent length scale ($\kappa_{\mathbf{G}}^{-1}$) such that $\kappa_{\mathbf{G}}=\kappa_0[(1+G^2/\kappa_0^2)]^{1/2}$. Within the context of the theory, higher-order Fourier components decay more rapidly. The temperature dependence of each order parameter at the surface was described by $\mathbf{G}$-dependent exponent.

The preceding calculations considered the simplest modification of the continuum free energy to incorporate the effect of a surface. There are other possibilities. For discrete systems, surface melting may proceed either continuously, for temperatures greater than the liquid-solid roughening temperature, or in a layer-by-layer fashion.[18] In materials where long-ranged forces are important, the thickness of the liquid layer may diverge as a power law.[19] In analogy to the phenomenology of wetting,[20] there may also occur surface premelting transitions, at which a disordered layer grows to a finite thickness discontinuously, or incomplete surface melting, where the liquid film thickness remains finite up to the melting transition.

A complementary theoretical approach to understanding surface disordering has been provided by molecular-dynamics (MD) simulations of crystal surfaces.[21–24] As an example, Schommers[22] examined the behavior of a Kr(001) surface using a realistic pair potential at $T=7$, 70, and 102 K [$T_t(\mathrm{Kr})=116$ K]. These results include a determination of root-mean-square displacements and of the relaxation of interlayer spacings in the near-surface layers. At low temperatures, the vibrational amplitudes perpendicular to the surface are larger than in the plane of the surface, but at $T=102$ K there is evidence that the surface layer is in a liquid state—in particular, atoms there experience diffusive motion. Simple two-body potentials are not adequate to describe metal surfaces, where metallic cohesion plays a dominant role.[23–25] To overcome this difficulty, empirical[23] and *ab initio*[24] potentials have been employed. Carnevali, Ercolessi, and Tosatti[23,27] simulated the Au(111) surface and found that the reconstructed surface remains stable up to the bulk melting temperature and beyond. In contrast, the topmost two layers of a hypothetical, unreconstructed Au(111) surface disorder below T_t. Stoltze, Nørskov, ad Londeman[24] studied the behavior of the Al(111) and Al(110) surfaces. They found evidence for disordering of the less densely packed Al(110) surface at temperatures significantly below the bulk melting temperature. The Al(111) surface was found to be ordered at all temperatures.

Experimentally, the most-studied material exhibiting surface disordering is Pb.[5,6,9,10,12,19,28,29] Ion-scattering experiments have shown that the Pb(110) surface is well ordered up to $T\sim450$ K. Between $T\sim450$ and 580 K this surface gradually disorders. For temperatures between $T\sim580$ K and $T_t(\mathrm{Pb})=600.8$ K, a liquid surface layer forms and its thickness increases in a manner consistent with the predictions of Ref. 15, eventually reaching a thickness of 25 layers 0.1 K below $T_t(\mathrm{Pb})$. Very near $T_t(\mathrm{Pb})$, subsequent measurements[19] suggest a crossover to a power-law temperature dependence for the growth of the fluid film, as expected for long-ranged interatomic forces. The crystal-face dependence of surface melting was investigated in Ref. 28. As might be expected, the more densely packed (111) facet does not undergo surface disordering. Other reports of surface melting behavior include the melting of ice[30] and the melting of thick adsorbed films on graphite substrates,[31] although the latter experiments are complicated by the possibility of triple-point wetting.[32,33]

The format of this paper is as follows. A discussion of

x-ray reflectivity from surfaces is given in Sec. II. In Sec. III, we present our results for the specular reflectivity. In Sec. IV, we present measurements of the overlayer reflectivity associated with the distorted-hexagonal reconstruction. Here, we make a comparison between our experimental results and the room temperature, structural predictions of Ercolessi, Tosatti, and Parrinello[34] based on MD simulations of the Au(001) surface—in particular, for the surface corrugations and interlayer spacings. In Sec. V, we extend consideration to the nonspecular (substrate) reflectivity for temperatures greater than the disordering temperature ($T > 1170$ K). Finally, we draw our conclusions in Sec. VI.

II. X-RAY SCATTERING FROM SURFACES

A. Cross-section, reflectivity, and real-space models

In this section, we discuss the x-ray intensity scattered from a crystal with a well-defined surface, including the effects of the spectrometer resolution. The reflectivity from an arbitrary unit cell is formulated and simplified to the (001) surface of a face-centered cubic (fcc) lattice. In the following, we consider scattering of monochromatic x rays from a sample in the standard four-circle geometry[35,36] with spectrometer angles 2θ, θ, χ, and ϕ. The incident and scattered x rays have wave vectors $\mathbf{k}_i$ and $\mathbf{k}_f$, respectively. The projections of these wave vectors within the scattering plane, defined by the concentric motions θ and 2θ of the goniometer, are described by the angles θ_1 and θ_2, respectively, while the deviations of these same wave vectors from the scattering plane are described by the angles ψ_1 and ψ_2, respectively. By construction, $\theta_1+\theta_2$ is equal to the scattering angle (2θ) and we use the standard convention that $\theta_1=0$ when the four-circle χ axis (orthogonal to the θ axis) is normal to the incident x-ray beam.[35] The probability that a photon is incident between θ_1 and $\theta_1+d\theta_1$ and between ψ_1 and $\psi_1+d\psi_{l1}$ is given by $g(\theta_1,\psi_1)d\theta_1 d\psi_1$. Under the assumption that all the incident x rays strike the sample, we have

$$\int g(\theta_1,\psi_1)d\theta_1 d\psi_1 = 1 \ . \tag{1}$$

After the sample, the x ray is scattered at an angle θ_2 in the diffraction plane and ψ_2 out of the diffraction plane and the detector acceptance is defined as $G(\theta_2,\psi_2)$. When limited by slits, the acceptance is unity within a range $\Delta\theta_2$ and $\Delta\psi_2$ and zero outside this range. With these definitions, the x ray intensity reflected into the detector I_s, normalized to the number of photons incident on the sample, I_0, is

$$\frac{I_s}{I_0} = \frac{1}{A_0}\int d\theta_1 d\theta_2 |T(\alpha)|^2 |T(\beta)|^2 d\psi_1 d\psi_2 \times g(\theta_1,\psi_1)G(\theta_2\psi_2)\left[\frac{d\sigma}{d\Omega}\right] , \tag{2}$$

where $d\sigma/d\Omega$ is the x-ray-scattering cross section, A_0 is the cross-sectional area of the beam, and α and β are the incident and exit angles, respectively. The Fresnel transmission coefficient describing the enhancement of the incident and scattered fields, $T(x)=2\sin x/[\sin x+(\cos^2 x_c-\cos^2 x)^{1/2}]$, is close to unity for the range of the present data and will be neglected in subsequent expressions.[37] (X_c is the critical angle for total external reflection.) Polarization effects are negligible for scattering in the vertical plane with synchrotron radiation sources and have also been ignored in the present analysis.

The x-ray cross section from a crystal with an ordered surface and real space lattice vectors **a**, **b** and **c** is given by

$$\frac{d\sigma}{d\Omega} = A\frac{(2\pi r_0)^2(\mathbf{c}\cdot\hat{\mathbf{n}})^2}{v^2}\left|\sum_{n=0}^{\infty} S_n(Q)e^{iQ_z z_n}\right|^2 \times \sum_{\tau_x\tau_y}\delta_{Q_x-H\tau_x}\delta_{Q_y-K\tau_y} , \tag{3}$$

where $r_0=2.818\times10^{-15}$ m is the Thomson radius, $v=(\mathbf{a}\times\mathbf{b})\cdot\mathbf{c}$ is the unit-cell volume, A is the illuminated surface area, $\hat{\mathbf{n}}$ is a unit vector in the surface-normal directions, and z_n is the z coordinate of the nth layer normal to the surface. In reciprocal space, the dimensions of the unit cell are τ_x, τ_y, and τ_z. Thus $Q_x=H\tau_x$ and $Q_y=K\tau_y$, where H and K are the usual Miller indices. We have incorporated the bulk Debye-Waller and form factors into the layer-dependent structure factor, which for the nth layer may be written

$$S_n(\mathbf{Q}) = \sum_{j=0}^{J-1} F_{j,n}(\mathbf{Q})e^{i\mathbf{Q}\cdot\mathbf{r}_{j,n}}e^{-W_{j,n}} . \tag{4}$$

$F_{j,n}$ is the form factor, $W_{j,n}$ is the Debye-Waller factor for the jth atom (in the nth unit cell), and we have assumed that there are J atoms per unit cell.

When the diffractometer is set to accept a particular τ_x, τ_y, and Q_z, we substitute Eq. (3) into Eq. (2) to find

$$\frac{I_s}{I_0} = \frac{A}{A_0}L_0(\Delta Q_z/\Delta\theta_1)\left|\frac{2\pi r_0(\mathbf{c}\cdot\hat{\mathbf{n}})}{v}\right|^2 \times \left|\sum_{n=0}^{\infty} S_n(\mathbf{Q})e^{iQ_z z_n}\right|^2 , \tag{5}$$

where $L_0=(k^3\sin 2\theta)^{-1}$ is the Lorentz factor and ΔQ_z is the range of Q_z that falls within the acceptance of the detector. In the nonspecular geometry, ΔQ_z may be limited either by the out-of-plane opening angle of the detector ($\Delta\psi_2$) at small Q_z, or by the in-plane opening angle of the detector ($\Delta\theta_2$) at large Q_z. It may be shown that the angles of incidence (α) and exit (β) are given by $\cos\alpha=\hat{\mathbf{n}}\cdot\hat{k}_i$ and $\cos\beta=\hat{\mathbf{n}}\cdot\hat{k}_f$. With the four-circle geometry, it is possible to set the spectrometer to collect data at an arbitrary wave-vector transfer and simultaneously impose the condition that the angles of incidence and exit be equal (i.e., $\alpha=\beta$).[36] This is done in the experiments reported here. Then, $\Delta Q_z=2k\cos\theta\sin\theta\Delta\theta_1/\sin\alpha$. This expression is appropriate only at large incident angles and provided that the longitudinal resolution is defined by $\Delta\theta_1$ and not by $\Delta\theta_2$. For typical samples (10 mm diam) and for grazing angles greater than several degrees, the size of the incident beam may be

chosen so that all of the incident beam impinges on the sample. In this case $A/A_0=1/\sin\alpha$, and we refer to the scattered intensity as the reflectivity (R):

$$R=\frac{I_s}{I_0}=\left|\frac{\pi r_0(\mathbf{c}\cdot\hat{\mathbf{n}})}{\nu Q_z}\right|^2\left|\sum_{n=0}^{\infty}S_n(\mathbf{Q})e^{iQ_z z_n}\right|^2. \quad (6)$$

It is important to note that the reflectivity need not depend on the instrumental parameters, so that absolute measurements are possible.

Up to this stage, we have considered an arbitrary unit cell. We now consider the unrelaxed, unreconstructed (001) surface of a primitive, fcc crystal with cubic lattice constant a. By unrelaxed, we mean that the interplanar spacing between top and second layers equals the bulk value. An unreconstructed surface is one in which the in-plane structure is identical to that of a bulk lattice plane. For the purpose of illustration, we take the surface Debye-Waller factor to be equal to its value in the bulk. Then, we may write

$$S(\mathbf{Q})=F(\mathbf{Q})e^{-W}s(H,K,L), \quad (7)$$

where $s(H,K,L)$ is the ordinary x-ray structure factor. Since H and K are integers, the structure factor simplifies to

$$s(H,K,L)=1+(-1)^{H+K}+[(-1)^H+(-1)^K]e^{i\pi L}. \quad (8)$$

For H and K both even, $|s(H,K,L)|$ is equal to $4\cos(\pi L/2)$; for H and K both odd, $|s(H,K,L)|$ is equal to $4\sin(\pi L/2)$; and for H even and K odd, and vice versa, the structure factor is zero. For an unrelaxed surface, all of the interlayer spacings are equal to the bulk interlayer spacing (d), i.e., $z_n=nd=an/2$. To calculate the reflectivity, we perform the sum over the half-space

$$\left|\sum_{n=0}^{\infty}e^{iQ_z dn}\right|^2=\frac{1}{4\sin^2(Q_z d/2)}. \quad (9)$$

Then, the specular and nonspecular reflectivities are obtained by substituting Eqs. (8) and (9) into Eq. (6):

$$R(\mathbf{Q})=\left|\frac{F(\mathbf{Q})e^{-W}}{2Q_z\sin(Q_z d/2)}\right|^2\left|\frac{2\pi r_0}{a^2}\right|^2 \quad (10)$$

for H and K even, and

$$R(\mathbf{Q})=\left|\frac{F(\mathbf{Q})e^{-W}}{2Q_z\cos(Q_z d/2)}\right|^2\left|\frac{2\pi r_0}{a^2}\right|^2 \quad (11)$$

for H and K odd.

For reconstructed or disordered surfaces the scattering amplitudes from each layer near the surface are no longer equivalent to those in the bulk. The reflectivity may then be written as

$$R(\mathbf{Q})=\left|\frac{F(\mathbf{Q})}{Q_z}\right|^2\left|\frac{2\pi r_0}{a^2}\right|^2 e^{-(\tau_x^2+\tau_y^2)\sigma_B^2}\times\left|\sum_{m=0}^{\infty}\rho_{\mathbf{G}}(m)e^{-Q_z^2\sigma_z^2(m)/2}e^{iQ_z d(m-\epsilon_m)}\right|^2, \quad (12)$$

where $\mathbf{G}$ is the projection of $\mathbf{Q}$ onto the surface plane and $\exp[-(\tau_x^2+\tau_y^2)\sigma_B^2]$ is the in-plane bulk Debye-Waller factor. In this expression, we have allowed for a layer-dependent surface-normal root-mean-square (rms) displacement amplitude $\sigma_z(m)$ and a relaxation ϵ_m, which is the fractional interlayer expansion with respect to the un-distorted bulk. For large m, the surface-normal displacement amplitude $\sigma_z(m)$ equals the bulk thermal vibrational amplitude obtained from the Debye-Waller factor. A displacement amplitude significantly different from the bulk thermal vibrational amplitude has a pronounced effect on the reflectivity if Q_z is far from a Bragg peak, but a minimal effect near Bragg peaks. The layer-dependent crystalline order parameter $\rho_{\mathbf{G}}(m)$ corresponds to the amplitude of the electron density wave of wave vector $\mathbf{G}$ for the mth layer. Thus, for specular reflectivity $\rho_{(0,0)}(m)$ is the mean density of the mth layer normalized with respect to the average bulk layer density. For nonzero $\mathbf{G}$, $\rho_{\mathbf{G}}(m)$ depends both on the lateral order (through $\mathbf{G}$) and the depth of the reconstructed or disordered surface region (through m). As we will show, the decay of $\rho_{\mathbf{G}}(m)$ near $m=0$ may significantly alter the nonspecular reflectivity for Q_z lying between bulk Bragg peaks, and especially near $Q_z=0$. It is worth noting that the definition of $\rho_{\mathbf{G}}(m)$ does not presuppose a particular structure for any layer, so that both reconstructed and unreconstructed layers may be accounted for through the dependence of these order parameters on the in-plane wave vector ($\mathbf{G}$). In the limit of large m, $\rho_{\mathbf{G}}(m)\to 1$ for $\mathbf{G}$ equal to any cubic wave vector, and $\rho_{\mathbf{G}}(m)\to 0$ for $\mathbf{G}$ equal to any wave vector associated with the hexagonal reconstruction.

B. Experiment

Experiments were performed at Cornell High Energy Synchrotron Source (CHESS) beamline A-2 and at National Sychrotron Light Source (NSLS) beamlines X20C and X22B. The experimental chamber has been described previously.[2,3] For the present experiments, the base pressure was 10^{-9} Torr at a sample temperature of $T=300$ K and 10^{-8} Torr at $T=1250$ K. From earlier experiments[1,3] we believe that clean Au(001) surfaces may be prepared and maintained at these base pressures and temperatures. A complete discussion of the sample preparation and characterization procedures has been given in Ref. 1. All measurements were performed in a vertical scattering geometry with $\lambda=1.59$ Å at X22B, $\lambda=1.45$ Å at X20C, and $\lambda=1.39$ Å at A-2. Data acquired at all three beamlines at $T=300$ K are identical and consistent with the results of our earlier rotating anode studies of the specular reflectivity of the Au(001) surface.[3] In the present work, performed at synchrotron sources, an absolute sensitivity of 10^{-9} was achieved. In contrast, sensitivities of only 10^{-7} were achieved using a rotating anode source.

The reflectivity measurements were carried out by rocking the sample about an axis perpendicular to the scattering plane with the spectrometer initially set to a position in reciprocal space (H,K,L), where $(H,K,0)$ corresponds to an allowed in-plane wave vector. The integrated intensity measured at the detector was then nor-

malized to the properly integrated direct beam intensity to obtain the absolute reflectivity.[2,3] Typical rocking curves obtained through the specular rod at the bulk-forbidden (0,0,1) position are shown inset in Fig. 2. They have a width of 0.1° full width at half maximum, which is half the width of the detector acceptance. This is expected for crystals with near-perfect mosaic and surface figure.

In these experiments, the incident and exit angles were held equal,[3] $\alpha=\beta$. The illuminated area of the sample was controlled by the incident slits (and not by the sample size), and the detector acceptance was determined by slits placed immediately before the detector. Detector slits were set to be 2 mm in the scattering plane and 10 mm out of the scattering plane and were located about 600 mm from the sample. The resultant resolution parallel to $\mathbf{Q}$ was $\Delta Q_{\parallel}/c^{*}\simeq 0.01$. The out-of-plane acceptance was set to be five times larger so that the entire fan of x rays scattered from the surface was collected. Near-grazing incidence $\Delta Q_z = k\Delta\Psi_2/\cos\alpha$ and the expression for the reflectivity given by Eq. (6) fails. We estimate that the crossover between these two regimes occurs at $\sin\alpha=\Delta\theta_1/\Delta\Psi_2$, which is at $Q_z/c^{*}\simeq 0.15$ for $\Delta\theta_1=5\times10^{-4}$ and $\Delta\Psi_2=2\times10^{-2}$.

III. SPECULAR REFLECTIVITY

In this section, we present the results of our measurements of the specular reflectivity and its dependence on sample temperature. As has been discussed in Sec. II, the specular reflectivity is sensitive to the average electron density along the surface-normal direction. It follows that analysis of the specular reflectivity is straightforward with simple real-space models. In a previous rotating anode study the x-ray specular reflectivity obtained from the Au(001) surface at $T=300$ K was interpreted in terms of a buckled, expanded, hexagonal overlayer.[3] With the additional flux (×1000) available at a synchrotron source, we have extended our measurements to larger wave vectors and to higher temperatures.

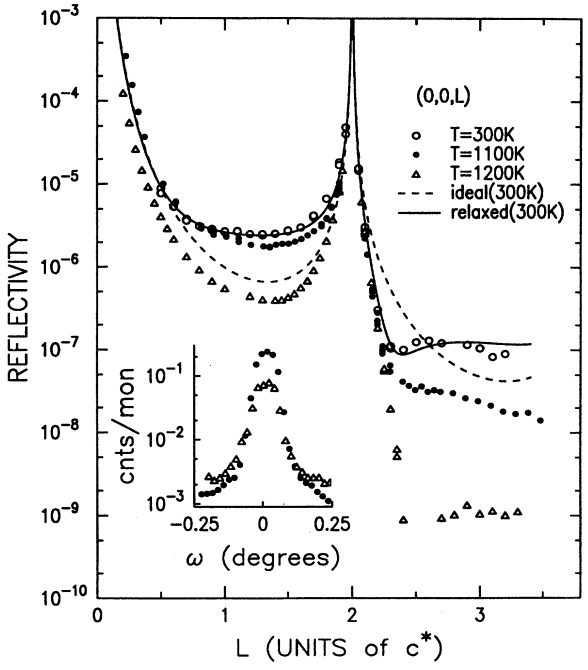

FIG. 2. X-ray specular reflectivity from the Au(001) surface. The dashed line is the predicted reflectivity for ideal termination. The solid line is the reflectivity for a reconstructed surface discussed in the text. Typical ω scans are shown in the inset.

The specular reflectivity obtained at temperatures $T=300$, 1100, and 1200 K is shown in Fig. 2. The main features of the profiles include an L^{-4} decrease at small L, characteristic of the Fresnel law of optics[2,35] and a sharp peak at $L=2$, which corresponds to the (0,0,2) Bragg reflection. In addition, there is a pronounced asymmetry in the intensity of the wings above and below the (0,0,2) Bragg reflection. Between $T=300$ and 1100 K the reflected intensity decreases so that above the (0,0,2) reflection the reflectivity measured at $T=1100$ K is about a factor of 5 smaller than the reflectivity measured at $T=300$ K. There is a much more dramatic decrease in the reflectivity in going from $T=1100$ to 1200 K. In particular, the intensity above $L=2$ decreases by more than a factor of 10 over this range.

The dashed line in Fig. 2 shows the profile predicted for the Au(001) surface at $T=300$ K from Eq. (10) assuming ideal bulk termination (i.e., no reconstruction or relaxation). It is clear that this profile does not represent the data at any temperature. On the other hand, the room-temperature reflectivity can be satisfactorily described, as in Ref. 3, by a model involving only a single layer with a structure different from that of bulk layers (solid line, Fig. 2). In this model the interlayer spacing between the top and second layer is expanded, $\epsilon_0=20\%$, the average top-layer density is increased, $\rho_{(0,0)}(0)=1.26$ (corresponding to a hexagonal overlayer), and there is a slightly enhanced surface displacement amplitude. This model, however, is inadequate at higher temperatures. In order to fit the reflectivity at the highest temperatures, it has been necessary to allow for a surface-normal rms displacement amplitude $\sigma_z(n)$ for several near-surface layers. For the purpose of analyzing the specular reflectivity, we take the displacement amplitude to include both the effects of enhanced surface vibrations and surface corrugation. Only by measuring the overlayer reflectivities together with the specular reflectivity has it been possible to separate these two contributions (see Sec. IV).

We have analyzed the specular reflectivity profiles from the Au(001) surface in the rotated, distorted-hexagonal phase at $T=300$ K (Fig. 3), in the distorted-hexagonal phase at $T=1100$ K (Fig. 4), and in the disordered phase at $T=1200$ K (Fig. 5). These profiles have been fit to Eq. (12). In the model, the scattering amplitude from each atomic layer is the product of the average layer density $\rho_{(0,0)}(m)$, the phase factor $\exp[iQ_z d(m-\epsilon_m)]$, and the factor containing the displacement amplitude $\exp[-Q_z^2\sigma_z^2(m)/2]$. For an ideal bulk layer the density $\rho_{(0,0)}(m)$ equals one, the relative interlayer expansion ϵ_m equals zero, and the displacement amplitude $\sigma_z(m)$ equals the bulk vibrational amplitude (σ_B). In the

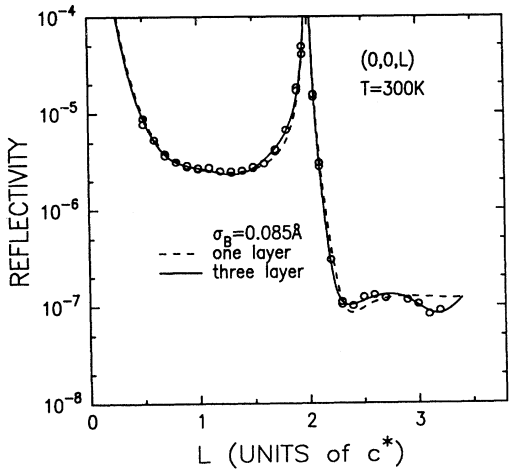

FIG. 3. X-ray specular reflectivity from the Au(001) surface at $T=300$ K. The model line shapes are discussed in the text.

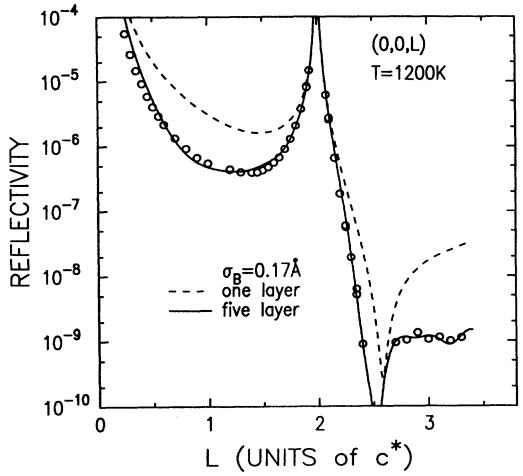

FIG. 5. X-ray specular reflectivity from the Au(001) surface at $T=1200$ K. The model line shapes are discussed in the text.

fitting, each time an additional layer was allowed to relax, ϵ_m and $\sigma_z(m)$ were varied for that layer. Except for the top layer density $\rho_{(0,0)}(m=0)$, which was allowed to vary, all other layer densities were fixed to 1.0. The data were then fit assuming first a single relaxed layer (single layer), and then assuming up to five relaxed layers (multilayer). For large m, we required that the displacement amplitude $\sigma_z(m)$ approach the bulk vibrational amplitude (σ_B) and we assumed that the temperature dependence of the bulk vibrational amplitude was given by $\sigma_B=0.085$ Å$\sqrt{T(K)/300K}$.[38] A review of the bulk Debye-Waller factor for gold has been prepared by Withrow, Barret, and Culbertson.[38]

The specular reflectivity was fit over the range $0.5<L<3.5$, excluding data within 0.02 of the Bragg peaks, and weighting each data point by the inverse of the measured reflectivity. The results obtained at room temperature are presented in Fig. 3. The fit to a single-layer reconstruction (dotted line) clearly describes the general features of the data at room temperature. The fitted parameters $\epsilon_0=0.20$, $\sigma_z(0)=0.32$ Å, and $\rho_{(0,0)}(0)=1.29$ are close to those obtained in the earlier, rotating anode study.[3] The surface displacement amplitude $\sigma_z(0)$ is larger than the bulk vibrational amplitude ($\sigma_B=0.085$ Å). By allowing the parameters for additional layers to vary in the model, it turned out that the parameters for the top layer were left nearly unchanged, and the fit was somewhat improved (solid line, Fig. 3). The best-fit parameters are summarized in Table I.

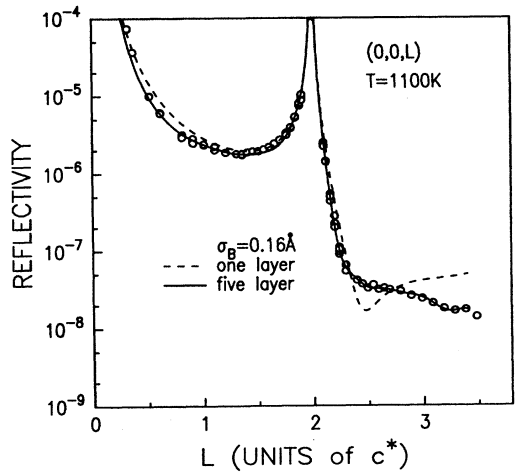

FIG. 4. X-ray specular reflectivity from the Au(001) surface at $T=1100$ K. The model line shapes are discussed in the text.

The specular reflectivity obtained at $T=1100$ K is shown by the open circles in Fig. 4. Although the hexagonal overlayer persists at $T=1100$ K, the domains rotated by 0.8° have now vanished.[1] From the high-resolution in-plane measurements[1] it is known that there is little change in the lattice constants of the hexagonal overlayer between $T=300$ and 1100 K. This suggests that the density of the overlayer remains constant. The results of fits of this data to a single-layer model with $\sigma_B=0.16$ Å (dashed line in Fig. 4) provide an inadequate description of the data above $L=2$. However, by varying both the displacement amplitudes for the top five layers and an interlayer expansion for the top two layers the fits were greatly improved, as shown by the solid line in Fig. 4. The best-fit values for the top-layer density and the interlayer spacings are close to those obtained at $T=300$ K. An important difference at $T=1100$ K is that the displacement amplitudes σ_z are significantly increased (Table I).

In going between $T=1100$ and 1200 K there is a dramatic decrease in the reflectivity profiles (Fig. 2), which is accompanied by the disappearance of the in-plane hexagonal peaks (see Ref. 1). Fits to a single-layer reconstruction (dashed line, Fig. 5) provide a poor description of the data, especially at large L. On the other hand, excellent fits are again obtained by varying the displacement amplitudes for several layers (as shown by

TABLE I. The rms surface displacement amplitudes, σ_z in angstroms, and relative interlayer expansion coefficients for the top layer and several succeeding layers derived from the analysis of the specular reflectivity. These parameters include the effect of thermal vibrations and surface corrugation. The parameters have been derived from fitting the specular reflectivity to Eq. (12) as described in Sec. III at $T=300$, 1100, and 1200 K. The asterisk denotes parameters that are held fixed.

Temp. (°C)	χ^2	$\rho_{(0,0)}$	σ_B (Å)	$\sigma_z(0)$ (Å)	$\sigma_z(1)$ (Å)	$\sigma_z(2)$ (Å)	$\sigma_z(3)$ (Å)	$\sigma_z(4)$ (Å)	ϵ_0	ϵ_1
300	0.04	1.29	0.085*	0.32	0.085*	0.085*	0.085*	0.085*	0.20*	0.0*
300	0.02	1.27	0.17	0.33	0.17*	0.17*	0.17*	0.17*	0.22	0.0*
300	0.008	1.25	0.085*	0.30	0.16	0.085	0.085	0.085	0.25	0.03
300	0.007	1.25	0.11	0.31	0.16	0.11	0.11	0.11	0.25	0.03
1100	0.5	1.50	0.16*	0.39	0.16*	0.16*	0.16*	0.16*	0.14	0.0*
1100	0.02	1.36	0.27	0.43	0.27*	0.27*	0.27*	0.27*	0.10	0.0*
1100	0.008	1.30	0.16*	0.38	0.31	0.25	0.21	0.17	0.21	0.03
1100	0.005	1.31	0.20	0.40	0.30	0.25	0.22	0.20	0.22	0.02
1200	82	1.58	0.17*	0.35	0.17*	0.17*	0.17*	0.17*	0.08	0.0*
1200	0.17	0.93	0.43	0.19	0.43*	0.43*	0.43*	0.43*	0.10	0.0*
1200	0.030	0.95	0.17*	0.48	0.35	0.29	0.23	0.19	0.13	0.03
1200	0.025	0.96	0.22	0.52	0.38	0.32	0.27	0.23	0.15	0.04

the solid line in Fig. 5). The best-fit parameters (Table I) at 1200 K for the surface displacement amplitudes are larger than at 1100 K—which suggests a more disordered surface above $T=1170$ K. In addition, the top layer density is closer to that of an ideally bulk terminated surface than to a close-packed hexagonal layer, whereas the interlayer expansion (10%) is intermediate between the values of the ideally terminated and reconstructed surfaces.

We have also fit the data to single- and multiple-layer models in which the bulk vibrational amplitude was varied (Table I). For the single-layer model, the fitted value is approximately twice the expected value. Reasonable values for the bulk vibrational amplitude are, however, obtained from the multiple-layer model (Table I). These fits appear indistinguishable from the multiple-layer model with a fixed bulk vibrational amplitude even though the fitted value is 10–20 % larger than expected.

Real-space density profiles along the [001] direction have been calculated from the multilayer fits with σ_B fixed at the bulk value, and are shown in Fig. 6 at $T=300$, 1100, and $T=1200$ K. The decrease in the peak height and the increase in the peak width for the top few layers is a direct consequence of larger rms displacement amplitudes at the surface. (For Fig. 6, the projected charge density was approximated by fitting the form factor of gold to a single Gaussian, which was then convolved with a Gaussian representing the distribution of surface displacement amplitudes.)

In summary, a detailed description of the density profile along the surface-normal direction has been obtained for the Au(001) surface between $T=300$ and 1200 K by analysis of the specular reflectivity. The surface-layer rms displacement amplitude obtained from the fitting procedure is significantly greater than the bulk thermal vibrational amplitude at all temperatures. In order to obtain satisfactory fits to the specular reflectivity at $T=1100$ and 1200 K, it was also necessary to include enhanced rms surface displacement amplitudes of four subsurface layers. (This includes both an enhanced vibrational amplitude and a corrugation amplitude.) The average surface density $\rho_{(0,0)}(0)$ decreases from about 1.3 at $T=1100$ K to approximately 1 at $T=1200$ K. Finally, the top-layer expansion $\epsilon_0-\epsilon_1$ decreases from about 0.20 at $T=1100$ K to about 0.10 at the highest temperatures.

IV. OVERLAYER REFLECTIVITY-SUBSURFACE CORRUGATION

As noted in Ref. 1 and shown in Fig. 1, an important feature of the distorted-hexagonal phase is the existence of satellite peaks about each hexagonal rod and truncation rod along the [110] direction. All of the satellite peaks may be indexed by a wave vector equal to the difference between the substrate in-plane wave vector $(1,1,0)c$ and the principal hexagonal wave vector $(1,0)h$. This suggests that both lattices—the hexagonal overlayer and the square substrate—are modulated. In this sec-

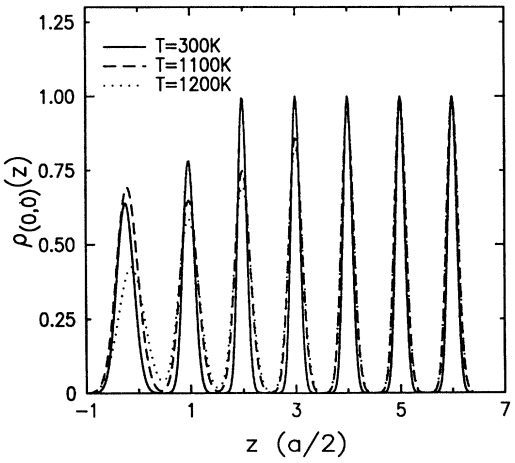

FIG. 6. Calculated electron density profiles vs depth obtained from fits to the specular reflectivity vs temperature. The peak density for the bulk material is normalized to unity at each temperature.

tion, we describe the results of overlayer reflectivity measurements which elucidate this modulation. The experiments were performed by setting the spectrometer to allowed in-plane wave vectors (see Fig. 1), and measuring the integrated intensity along the surface-normal direction (L). In the rotated, distorted-hexagonal phase the intensities from both rotated and unrotated domains were summed. In the following, we distinguish between two different contributions to the surface-normal displacement amplitude $\sigma_z(n)$ and include both a layer-dependent corrugation amplitude (ζ_n) and a surface-normal vibrational amplitude [$\sigma_z'(n)$].

The overlayer reflectivities obtained at the principal hexagonal wave vectors $(1,0,L)h$ at $T=300$ and 1100 K and at $(0,1,L)h$ at 300 K are shown in Fig. 7. As discussed in Ref. 1, it is convenient to express the scattering from the distorted-hexagonal overlayer in hexagonal coordinates. We denote the principal hexagonal wave vectors $(1,0,L)h \equiv (1.207,1.207,L)c$ and $(0,1,L)h = (1,0,L)h\ R\,(120°)$ (see Fig. 1). (The latter coordinate is not oriented along a cubic symmetry direction.) As may be seen in Fig. 7, the overlayer reflectivity decreases with increasing L, falling off somewhat faster than L^{-2}. There are no sharp peaks at any L, however, these profiles appear weakly modulated. As the temperature is increased from $T=300$ K (open circles) to $T=1100$ K (solid circles), the reflectivity decreases. We believe that the decrease in reflectivity with increasing temperature occurs as a result of increased vibrational amplitudes. The measured $(1,1,L)h$ (not shown in Fig. 7) and $(0,1,L)h$ rods are indistinguishable at all temperatures below $T=1170$ K.

Under the assumption that only a single undistorted layer contributes to the scattering at the primary hexagonal positions, Eq. (12) for the reflectivity reduces to

$$R(\mathbf{Q})=\frac{1}{2}\left|\frac{\rho_{(0,1)h}F(\mathbf{Q})e^{-W}}{Q_z}\right|^2\left|\frac{2\pi r_0}{a^2}\right|^2. \tag{13}$$

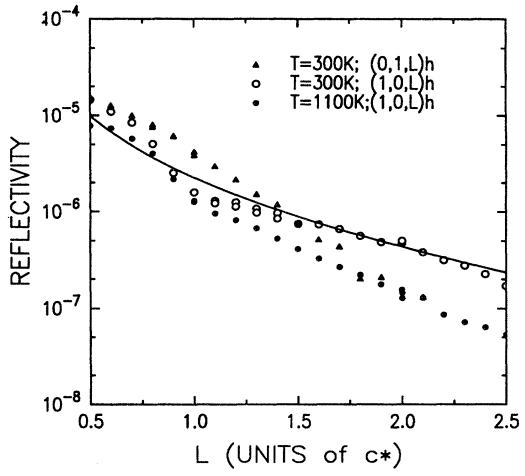

FIG. 7. Overlayer reflectivity profiles for the primary hexagonal peaks of the Au(001) surface. The solid line is the reflectivity calculated from Eq. (13), for an undistorted hexagonal overlayer with no bulk relaxations.

We assume $\rho(0,1)h\,(n=0)\simeq 1.26$ for the hexagonal overlayer. The factor of $\frac{1}{2}$ arises because there are two symmetry equivalent [110] directions. The reflectivity expected for an undistorted, hexagonal monolayer is shown by the solid line in Fig. 7. As may be seen, Eq. 13 describes the overall Q_z dependence quite well. However, there are clear deviations (discussed in more detail below) which we believe result from subsurface relaxations. (Deviations at small L in Fig. 7 result from incorrectly integrating reflectivity as discussed in Sec. II. Therefore data obtained for L less than 0.8 have been eliminated in the analysis.)

The reflectivity at the principal modulation wave vector (δ,δ,L) is shown in Fig. 8, along with the reflectivity at the principal hexagonal position $(1,0,L)h$ at $T=1100$ K. The most striking feature of the reflectivity along (δ,δ,L) is the broad peak near $L=2$. In the absence of a modulation, the intensity along this rod would be zero. If only one layer were modulated with in-plane wave vector $(\delta,\delta,0)$, then the reflectivity along (δ,δ,L) would exhibit a monotonic decay (dashed line, Fig. 8). In order for this rod to develop a peak, as observed, more than a single layer must contribute to the scattering.

A second important feature of the reflectivity along (δ,δ,L) is that the average L dependence (dashed lines in Fig. 8) is weaker than for $(1,0,L)h$. In this regard, the absence of a significant increase of the reflectivity at small L along (δ,δ,L) suggests that the modulation is a corrugation with the atomic displacements perpendicular to the surface. To model this, we assume that a corrugation may be formally approximated as a one-dimensional sinusoidal displacement of the atoms along the surface

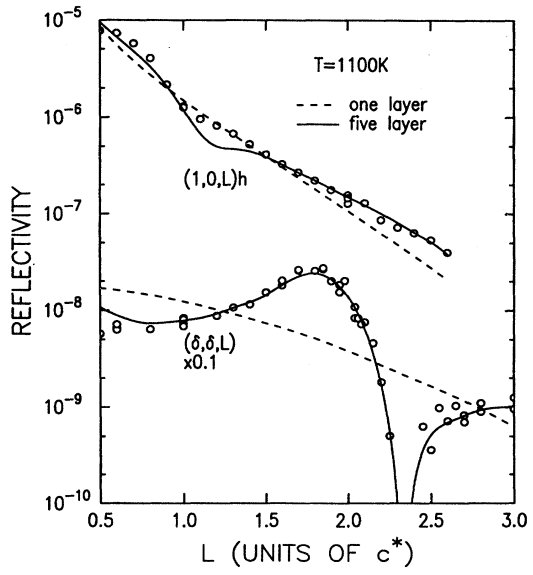

FIG. 8. Overlayer reflectivity from the Au(001) surface at $T=1100$ K. The solid line is the result of fitting the $(0,0,L)$, $(1,0,L)$, and (δ,δ,L) reflectivities simultaneously to the model described in the text. A single corrugated layer, dashed lined, does not describe the (δ,δ,L) rod.

normal direction $\hat{z}$, with amplitude ζ_n. Specifically, we include in the layer-dependent structure factor a displacement $u_{jn}=\zeta_n\hat{z}\sin(\boldsymbol{\delta}\cdot\mathbf{r}_{j,n})$, where $\mathbf{r}_{j,n}$ is the jth atom in the nth layer and $\boldsymbol{\delta}=(\delta,\delta,0)_c$ is the incommensurability. Previous helium scattering studies[39] and x-ray specular reflectivity studies[3] have considered a single corrugated layer. Here, we allow the amplitude of the distortion ζ_n to propagate several layers into the bulk. For a sinusoidal distortion, the layer-dependent crystalline order parameter for the nth layer, $\rho_G(n)$, may be modeled using Bessel functions (see Ref. 40), that is,

$$\rho_G(n)\propto J_m(Q_z\zeta_n)\ , \tag{14}$$

where J_m is the mth-order Bessell function. Then, using Eq. (12), the overlayer reflectivities for the $(\delta,\delta,L)_c$ and $(1,0,L)h$ rods are[40]

$$R(\delta,\delta,L)=\left|\frac{F(\mathbf{Q})}{Q_z}\right|^2\left|\frac{2\pi r_0}{a^2}\right|^2\left|J_1(\zeta_0Q_z)(1.26)e^{-Q_z^2\sigma_z'^2(0)/2}e^{-iQ_zd\epsilon_0}+\sum_{n=1}^{N}J_1(\zeta_nQ_z)e^{-Q_z^2\sigma_z'^2(n)/2}e^{iQ_zd(n-\epsilon_n)}\right|^2$$

and

$$R(1,0,L)=\left|\frac{F(\mathbf{Q})}{Q_z}\right|^2\left|\frac{2\pi r_0}{a^2}\right|^2\left|J_0(\zeta_0Q_z)e^{-Q_z^2\sigma_z'^2(0)/2}e^{-iQ_zd\epsilon_0}+\sum_{n=1}^{N}iJ_1(\zeta_nQ_z)e^{-Q_z^2\sigma_z'^2(n)/2}e^{iQ_zd(n-\epsilon_n)}\right|^2, \tag{15}$$

where five layers are included in the analysis ($N=4$). The first term in each of these sums is the contribution from the incommensurate hexagonal overlayer, while the remaining terms are the contributions from the substrate layers which support an incommensurate corrugation. It is important to note that in the limit of small Q_z the measured reflectivity at (δ,δ,L) in Fig. 8 is approximately independent of Q_z, in contrast to the reflectivity at $(1,0,L)h$, which decreases roughly as $(1/Q_z)^2$. This behavior follows analytically from the small-argument limit of the mth-order Bessel function, confirming that the corrugation amplitude ζ_n lies principally along $\hat{z}$. Note that in the model we have also allowed for surface-normal vibrational amplitudes $\sigma_z'(n)$ and an interlayer expansion ϵ_n. It is possible, therefore, to determine independently both the corrugation amplitude and the surface-normal vibrational amplitude. In the analysis of the specular reflectivity discussed in Sec. III, these two contributions were included together in the surface-normal displacement amplitude $\sigma_z'(n)$.

We have fit the reflectivities along the rods at $(0,0,L)$, $(1,0,L)h$, and (δ,δ,L) obtained at 1100 K to Eq. (15) allowing $\zeta(n)$ and $\sigma_z'(n)$ to vary. In Fig. 8, the results of the fits are shown by solid lines. The resultant best fit parameters are $\epsilon_0=0.23$, $\epsilon_1=0.03$; $\zeta(0-3)=0.31$, 0.21, 0.10, and 0.04 Å; and $\sigma_z'(0-3)=0.32$, 0.20, 0.19, and 0.17 Å. As before, the surface vibrational amplitude approaches that for the bulk Debye-Waller factor of 0.16 Å, as n becomes large. The fit provides an excellent representation of the rods at $(0,0,L)$ and (δ,δ,L), but there are deviations for the rod at $(1,0,L)h$. Specifically, while the data and the fit each display a dip, the position and depth of the dip are not in precise agreement. It is clear, however, that if subsurface corrugation is not included in the analysis, so that only the top layer is corrugated, the resultant line shape decreases monotonically (dashed lines, Fig. 8) and *fails* to describe the nonspecular reflectivity. It follows that the "rigid substrate" approximation, in which the substrate is regarded as undistorted in the reconstruction, provides an inadequate description of the structure of Au(001) surface.

We were unable to observe intensity scattered at $(2\delta,2\delta,L)$ and at $(1-2\delta,1-2\delta,L)$ for any L at $T=300$ and 1100 K. The absence of higher harmonics supports our assumption that the corrugation is primarily sinusoidal, and suggests that the in-plane displacements along the [110] direction are weak. Further modeling has confirmed that deviation from uniform spacing of just a few percent would give rise to observable peaks at these positions.

To carry the analysis further (that is away from the [110] axis), we have developed an atomistic model of the in-plane structure. As emphasized in Ref. 1, the Au(001) top layer is incommensurate with respect to the underlying bulk and therefore cannot be described by a simple real-space model. However, if the reconstruction is composed of a sufficiently simple motif, such as a structure which is locally fivefold commensurate, then the reflectivities can be calculated using this motif and compared to the measured results. Guided by this observation, we have developed a unit cell with six atoms in the top layer and five atoms in subsequent layers. It turns out that along the [110] direction, the uniaxial incommensurate model discussed above and the atomistic model discussed below give identical results for the reflectivity, if it is assumed that the modulation is purely sinusoidal. We emphasize that our goal in the following is mainly to examine the surface corrugation and vibrational amplitudes, and not to deduce in-plane atomic positions.

Specifically, we define a unit cell in which there are six uniformly spaced atoms (initially) in the top layer, arranged on a triangular lattice. We also assume a sinusoidal corrugation (ζ_n) with a wave vector (0.2,0.2,0),

increased vibrational amplitudes $[\sigma_z'(n)]$, and an interlayer relaxation (ϵ_n). (The bulk vibrational amplitude was fixed at the bulk valve). Undistorted positions of the bulk atoms, in a coordinate system where (1,0,0) is equivalent to (1,1,0) $a/\sqrt{2}$, and (0,1,0) is equivalent to $(1,\bar{1},0)a\sqrt{2}$, are given by (1,−2,0), (1,−1,0), (1,0,0), (1,1,0), and (1,2,0) for even layers. The positions are decremented by (0,0.5,0) for odd layers. For the top layer ($n=0$), the atomic positions are given by (1.25,−2.08,0), (0.75,−1.25,0), (1.25,−0.42,0), (0.75,0.42,0), (1.25,1.25,0), and (0.75,2.08,0). A small distortion (less than 0.1) in the position of the atoms in the second layer along the [110] direction helps to explain some of the differences between the $(1,0,L)h$ and $(0,1,L)h$ rods. The uncertainty of this distortion obtained from the least-squares analysis, however, is nearly as large as the distortion.

Specular and nonspecular reflectivities obtained at $T=1100$ and 300 K for six rods and hundreds of data points were then simultaneously fit to this model. The results of the fitting at $T=1100$ K are shown by solid lines in Fig. 9. The corrugation parameters obtained at $T=1100$ K, $\zeta(0-3)=0.28$, 0.14, 0.06, and 0.02 Å, are close to the values obtained from fits to Eq. (15). A real-space depiction of the surface corrugation generated by these parameters is shown in Fig. 10. For comparison,

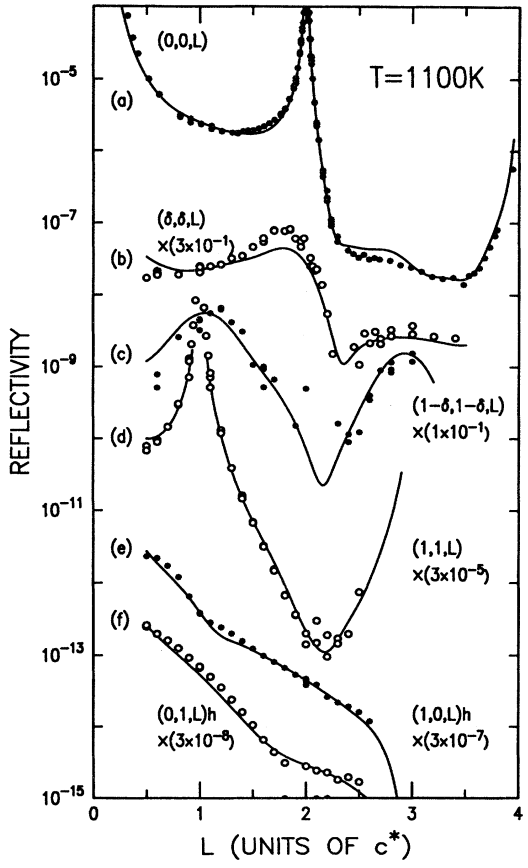

FIG. 9. Absolute reflectivity of Au(001) at T=1100 K for various different in-plane wave vectors. The solid lines are fits to a (5×1) unit cell model as described in the text.

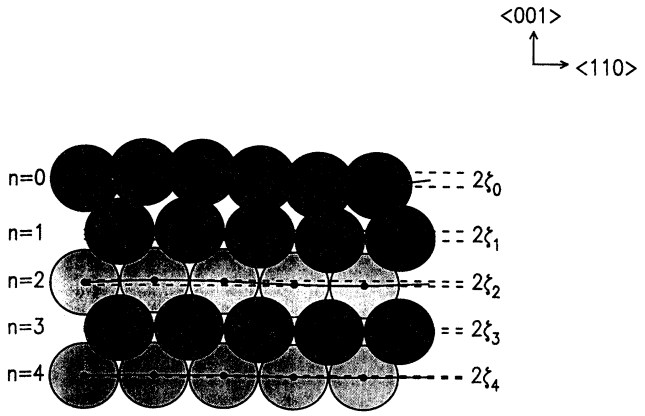

FIG. 10. Real-space model of the Au(001) surface corrugation.

helium diffraction measurements of the Au(001) surface yield a top-layer corrugation amplitude of $\zeta_0=0.235$ Å (Ref. 39) (0.47 Å peak to peak). In a related effort, Ercolessi, Tosatti, and Parrinello[34] calculated the corrugation amplitudes using a "glue Hamiltonian" with a (34×5) unit cell. They have reported corrugation amplitudes of $\zeta(0-3)=0.235$, 0.105, 0.065, and 0.04 Å. Thus our fitted top-layer corrugation amplitude $\zeta_0=0.28$ Å, is in close agreement with previous experimental[39] and theoretical[34] results. However, Ercolessi, Tosatti, and Parrinello also predict a top-layer expansion of 3.6%, whereas our reflectivity measurements convincingly show an expansion of 20±3%.

It is also possible to describe the measured dependence of ζ_n on the distance from the surface (z_n) using an exponential decay $\zeta_n=\zeta_0\exp(-z_n/\lambda)$. Fitting ζ_n at $T=1100$ K (see Fig. 8), we find $\zeta_0=0.28\pm0.02$ Å with $\lambda=3.3\pm0.6$ Å. This form is consistent with the measured values of the corrugation amplitude as shown by the open circles in Fig. 11. Simple elasticity theory leads

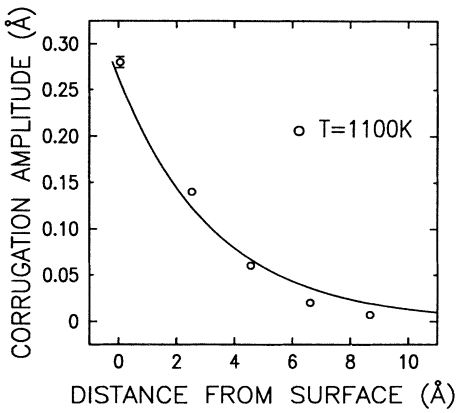

FIG. 11. Corrugation amplitude ζ_n vs the distance from the surface at $T=1100$ K. Open circles are fitted corrugation amplitudes and solid lines correspond to exponential decay of amplitude discussed in the text.

TABLE II. The thermal rms amplitudes derived by simultaneously fitting the specular, nonspecular and overlayer reflectivity profiles. The results at $T=300$ K and 1100 K are discussed in Sec. IV. The results at $T=1200$ K are discussed in Sec. V.

Temp. (°C)	0	1	2	3	4	Bulk
300	0.18	0.19	0.15	0.10	0.085	0.085
1100	0.31	0.25	0.21	0.18	0.17	0.16
1200	0.48	0.35	0.29	0.23	0.19	0.17

one to expect that λ be of the order of the modulation wavelength divided by 2π, i.e., 2.3 Å.

The main differences between the overlayer reflectivity observed at $T=300$ K and that at $T=1100$ K are attributable to an increase of the surface-normal vibrational amplitudes (see, for example, Fig. 7). Allowing the corrugation amplitudes to vary in the analysis at $T=300$ K yielded values indistinguishable from the results at $T=1100$ K. In order to extract changes in the vibrational amplitudes we have fixed the corrugation amplitudes at $T=300$ K to the values obtained at $T=1100$ K. The corresponding vibrational amplitudes obtained at $T=300$ K are given in Table II, along with the results of fitting the profiles obtained at $T=1100$ K. In the hexagonal phases ($T=300$ and 1100 K), the vibrational amplitudes $\sigma_z'(n)$ are about twice the bulk value. Comparable enhancements in the surface-normal vibrational amplitudes have been predicted for the (001) surface of krypton[22] using molecular-dynamic simulations far from the melting point. For the closed-packed, reconstructed Au(111) (Ref. 23) surface simulations predict an enhancement of 1.5 at temperatures close to the melting point.

In summary, measurements of the overlayer reflectivities have led to a model of the Au(001) surface in which the top, hexagonal layer is corrugated with an incommensurate wave vector $(\delta,\delta,0)_c$. To explain both the small-Q_z behavior of the rod at $(\delta,\delta,L)_c$ and the finite-Q_z modulations of the rods at $(1,0,L)h$ and $(\delta,\delta,L)h$, it has been necessary to consider a structure in which up to five succeeding substrate layers are also corrugated (with the same wave vector), but with an amplitude which decays exponentially with depth.

V. NONSPECULAR REFLECTIVITY-SURFACE DISORDERING

In this section, we discuss the nonspecular reflectivities obtained for the Au(001) surface for temperatures above $T=1170$ K. As discussed in Ref. 1 and in Sec. III, the intensities of the in-plane hexagonal reflections disappear and the specular reflectivity decreases dramatically in this phase. We have argued that this behavior is consistent with a disordering transition of the top, and possibly succeeding, layers. The profiles of the nonspecular reflectivity are particularly useful since they directly probe the crystalline order parameter $\rho_G(n)$. Specifically, in the high-temperature phase above 1170 K, the deviations of the order parameter from unity, $|\rho_G(n)|<1$, for substrate wave vectors **G**, measure the degree of disorder of the nth layer. To study these effects in detail, we have carried out absolute, nonspecular reflectivity studies along the $(1,1,L)$ and $(2,0,L)$ truncation rods above and below the hexagonal disordering transition.

Nonspecular reflectivity was obtained at $T=300$, 1100, 1150, 1200, and 1250 K for the $(1,1,L)$ and $(2,0,L)$ rods, as shown in Figs. 12 and 13. As with the specular reflectivity (Fig. 3–5), each data point represents an integrated intensity[3] obtained by rocking the sample through ω and subtracting the background. Typical rocking curves (transverse scans) of the specular reflectivity and of the substrate reflectivity along the $(1,1,L)$ direction are shown at $T=1100$ and 1250 K in Fig. 14. It is clear from Fig. 14 that to within the present counting statistics and resolution, no change in the transverse line shapes is observed above $T=1170$ K. This suggests that to within the x-ray coherence area, the surface remains a smooth facet.

Referring now to Figs. 12 and 13, it is clear that the reflectivity is too weak, and the background too large, to carry out reliable measurements between neighboring Bragg peaks at the highest temperatures. Nevertheless, important features emerge from the $(1,1,L)$ reflectivity profiles. First, at each temperature the nonspecular profile is considerably more symmetric about the Bragg peaks than is its specular counterpart. Second, as the temperature is raised, the reflectivity decreases by about a factor of 100 at (1,1,0.5) (see Fig. 12). The corresponding change in the specular reflectivity at (0,0,0.5) (see Fig. 2) is much smaller ($\times 5$). We highlight the behavior at small Q_z in Fig. 15, which shows the ratio of the reflectivity obtained along the $(1,1,L)$ direction at $T=1250$ K to that obtained at $T=1100$ K. At the smallest Q_z studied ($Q_z \sim 0.15c^*$), the ratio is reduced by

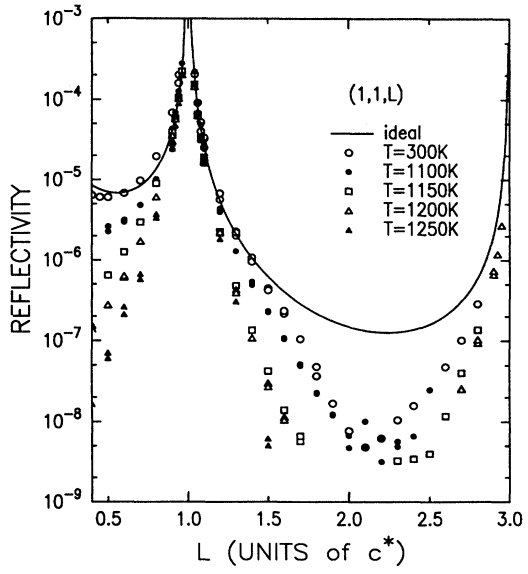

FIG. 12. Nonspecular reflectivity along the $(1,1,L)$ direction at several temperatures. The solid line is the calculated reflectivity for an ideally terminated surface.

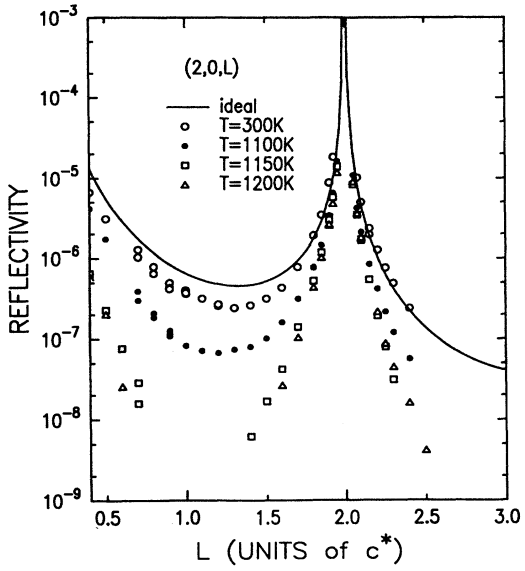

FIG. 13. Nonspecular reflectivity along the $(2,0,L)$ direction at different temperatures. The solid line is the calculated reflectivity for an ideally terminated surface.

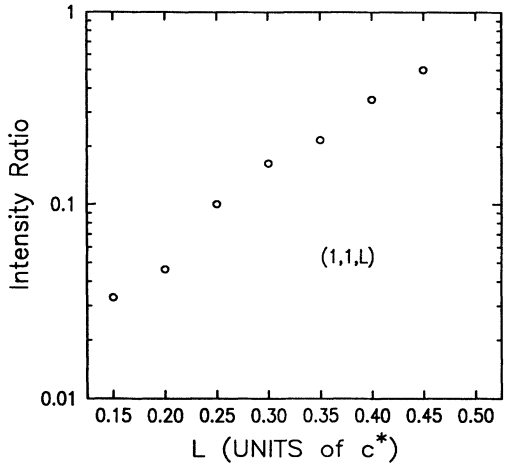

FIG. 15. Ratio of the intensity obtained along the $(1,1,L)$ direction at $T=1200$ K to that at $T=1100$ K.

about a factor of 30. Referring to Eq. (12) it may be seen that the nonspecular reflectivity is most sensitive to lateral disorder ($|\rho_G|<1$) for Q_z near zero, where the influence of the interlayer spacing ϵ_m and surface displacement amplitudes $\sigma_z(m)$ are minimal. In addition, the change in the bulk vibrational amplitude from 0.16 ($T=1100$ K) to 0.17 Å ($T=1200$ K) reduces the reflectivity by a negligible amount. Therefore, in order to understand the large decrease in the reflectivity at (1,1,0.5) in going from $T=1100$ to 1200 K we are led to consider models of the surface structure which incorporate lateral disorder at the highest temperatures ($T>1170$ K).

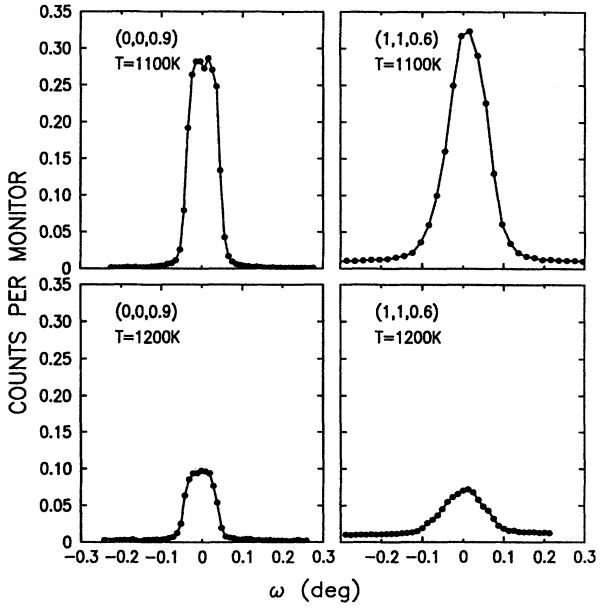

FIG. 14. Rocking curves through specular and nonspecular reciprocal wave vectors at $T=1100$ and 1200 K. There are no evident changes in the profiles shapes with temperature.

The calculated nonspecular reflectivity for an ideally terminated surface is shown by the solid lines in Figs. 12 and 13. At all temperatures the measured reflectivity lies below the solid lines with the largest differences occurring at the highest temperatures. As shown in Sec. IV, these deviations can be understood on the basis of the hexagonal reconstruction for temperatures less than 1170 K. However, for temperatures greater than 1170 K the surface diffraction pattern has the (1×1) symmetry characteristic of the unreconstructed bulk. In the following we have fit the $(1,1,L)$ and $(2,0,L)$ rods to the same model as used for the specular reflectivity, Eq. (12), in which each layer is described by a displacement amplitude $[\sigma_z(m)]$, an expansion parameter (ϵ_m), and a crystalline order parameter $[\rho_G(m)]$. Since we expect that ϵ_m and σ_z should be the same for specular and nonspecular reflectivities, we have fixed these parameters to the values obtained from the fits to the specular reflectivity at each temperature discussed in Sec. III (see Table I). The solid lines in Figs. 12 and 13 for an ideally terminated surface correspond to $\epsilon_m=0$, $\sigma_z(m)=\sigma_B$, and $\rho_G(m)=1$.

The integrated intensities measured along the $(1,1,L)$ truncation rod at $T=300$, 1100, and 1200 K are collected in Fig. 16 along with fits to different models of the crystalline order parameter $\rho_{(1,1)}$. The calculated reflectivities for an ideally terminated crystal are shown by the dotted lines. This model describes the data at $T=300$ K over the range $0.5<L<1.5$. Beyond this range, however, there are noticeable deviations and by $T=1100$ K this simple model deviates even in the wings of the Bragg peaks. At $T=1200$ K the intensity observed at $Q_z=0.5$ is more than a factor of 10 lower than predicted for ideal termination.

Our next approach in describing the data was to assume that the crystalline order parameter decays as a Gaussian:

$$\rho_G(n)=\exp-\left[\frac{|G|^2[\sigma_z^2(n)-\sigma_B^2]}{2}\right]. \quad (16)$$

When this term is combined in Eq. (12) with the term for the surface-normal vibrational amplitude, the net vibrational amplitude is isotropic. For $T=300$ and 1100 K, we set $\rho_{(1,1)}(0)=0$ since the hexagonal surface layer is incommensurate with the bulk. As may be seen in Fig. 16, the isotropic approximation does not alter the fits for $T=300$ K since $\sigma_z|\mathbf{G}| \ll 1$; it does, however, provide a better representation at $T=1100$ K (dashed line). Nevertheless, the measured reflectivity decreases dramatically (see Fig. 12) in going from $T=1100$ to 1200 K—more than may be accounted for by the corresponding change in the surface-normal displacement amplitudes $[\sigma_z(n)]$ obtained from the fits to the specular reflectivity. For this reason, the isotropic approximation fails to describe the data adequately at $T=1200$ K (dashed line in Fig. 16).

In order to describe the results at the highest temperatures, we have explicitly included disordered near-surface layers by modeling the crystalline order parameter ρ_G by an error function

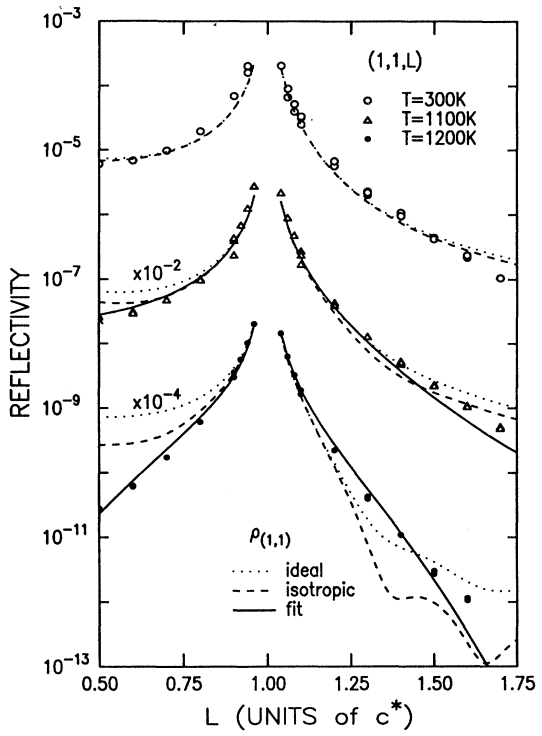

FIG. 16. Nonspecular x-ray reflectivity along the $(1,1,L)$ direction at $T=300$, 1100, and 1200 K. The reflectivity calculated using the parameters obtained from the analysis of the specular reflectivity is shown by the dotted lines. The calculated reflectivities from an isotropic model of the surface vibrational amplitudes are shown by dashed lines. Fits to a disordered surface region, Eq. (16), are shown as solid lines.

$$|\rho_G(z)|=\frac{1}{2}\left[1-\mathrm{erf}\left[\frac{z-D}{W}\right]\right]. \quad (17)$$

According to this model, the disordered region extends from the surface at $z=0$, where $\rho_G \simeq 0$, to $z=D$ since at this position $\rho_G=1/2$. The width of the interface between ordered and disordered regions is given by W. It should be noted that the essential features of the model can be equally well represented by other functional forms. In particular, to within the confidence limits of the present analysis, the decay of ρ_G with z can be satisfactorily described by a hyperbolic form and similar values of the thickness of the disordered region and of the width of the transition region result.[13]

At $T=1100$ and 1200 K the $(1,1,L)$ rods have been fit to Eq. (12) over the range $0.5<L<1.5$ by inserting the best-fit parameters obtained from the specular reflectivity for ϵ_m and $\sigma_G(n)$ (see Table I), using Eq. (17) for $\rho_G(n)$, and by varying W and D. The resulting fits are shown by the solid lines in Fig. 16. At all temperatures the use of an error function for $\rho_{(1,1)}$ improves the description of the data by further reducing the reflectivity at $T=1100$ and 1200 K in the wings of the Bragg peak. (It is important to recall that for $T<1170$ K we have already described the nonspecular reflectivity on the basis of the hexagonal reconstruction discussed in Sec. IV.) As a result of the fitting, we find $W=1.5\pm0.2$ Å and $D=3.0\pm2.0$ Å at 1100 K and $W=3.3\pm0.2$ Å and $D=5.03\pm3.0$ Å at 1200 K, which is suggestive of a disordered surface region for $T>1170$ K. It is noteworthy that the fits are more sensitive to the width of the interface between ordered and disordered regions than to the thickness of the disordered region. The dependence of $\rho_{(1,1)}$ on distance from the surface is shown in Fig. 17 for $T=300$, 1100, and 1200 K. From the figure it is seen that the reduction of the reflectivity above $T=1170$ K is associated with the decay of the sharp interface in real space, consistent with 1–2 disordered surface layers.

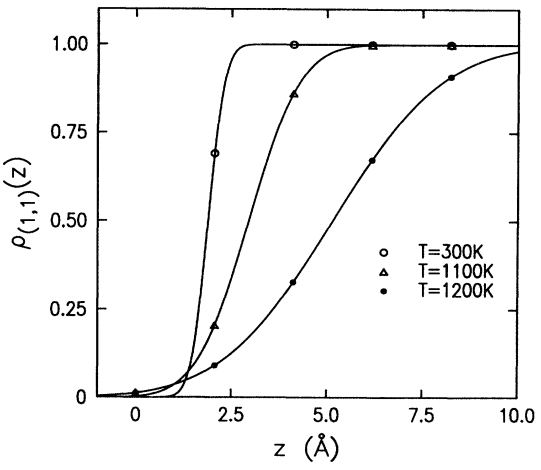

FIG. 17. Layer-dependent crystalline order parameter $\rho_{(1,1)}$ obtained from fits to Eq. (16).

The nonspecular reflectivity along $(2,0,L)$ is shown by the open circles at $T=1200$ K in Fig. 18. The reflectivity calculated from Eq. (12) using the parameters from the fit to the $(1,1,L)$ rod (see above) is shown by the dashed line. A better description of the $(2,0,L)$ data is obtained by allowing W and D to again vary in the fitting procedure. The parameters obtained are $W=4.2\pm0.4$ Å and $D=5.0\pm3.0$ Å.

On the basis of the results presented so far, it seems reasonable to conclude that the top and possibly one or two succeeding layers of the Au(001) surface are structurally disordered at temperatures between $T=1170$ and 1250 K. In order to distinguish among different possible models of disordered near-surface layers, we attempted to detect the weak ring pattern expected from liquid or melted overlayers.[9,10,32] Measurements were performed at fixed $L=0.5$ to prevent the beam from spilling off the sample. Radial scans were then performed at temperatures above and below $T=1170$ K at several azimuthal angles. The primary features of the scans performed at high temperatures included broad, weak peaks, which we were able to identify with diffuse scattering from the (1,1,1) and (2,2,2) bulk reflections. These features were unchanged for temperatures below $T=1170$ K.

In summary, the x-ray diffraction pattern obtained for the Au(001) surface at elevated temperature is characterized, in part, by the abrupt disappearance of the hexagonal order above $T=1170$ K[1]. From analysis of the specular reflectivity, we have found that the average top-layer density is decreased from the hexagonal value of $\rho_{(0,0)}(0)\sim1.26$ below $T=1170$ K to a value nearer the bulk density $\rho_{(0,0)}\sim1$ above $T=1170$ K. In addition, we have found that the surface-normal vibrational amplitudes $\sigma_z'(n)$ abruptly increase above $T=1170$ K. Except for their amplitudes, the transverse line shapes obtained in specular reflectivity measurements seem little changed for temperatures above or below the hexagonal disordering transition, suggesting that the surface remains smooth. (Better statistics will be required before a detailed line-shape analysis is warranted.) From the sharp decrease of the nonspecular reflectivity, we have deduced that the in-plane crystalline order parameter $|\rho_G|<1$ in the first one to two layers above $T=1200$ K, consistent with decreased lateral order. We have been unable, however, to detect the weak scattering associated with a two-dimensional liquid. We are unable, on the basis of our data, therefore, to distinguish between, for example, a two-dimensional isotropic liquid, or a structure which is more properly viewed as crystalline layers with enhanced lateral vibrations. It should be pointed out, however, that even though the surface is disordered in plane, surface atoms appear to reside in well-defined layers, since the rms displacements are always much smaller than the separation between atomic planes. These observations are consistent with molecular-dynamic simulations of the Al(110) surface[24] and of the Kr(001) surface.[22] In contrast to these results at the (001) surface, there is no corresponding evidence for microscopic surface disordering at the (111) face of gold.[27] It seems clear that experiments closer to the triple point and with larger in-plane wave vectors will be required to further elucidate the nature of the disordered surface region. Complementary x-ray-scatter experiments performed under electrochemical conditions have shown the Au(001) surface forms a hexagonal reconstruction when a negative potential is applied and that the reconstruction is lifted for positive potentials.[41]

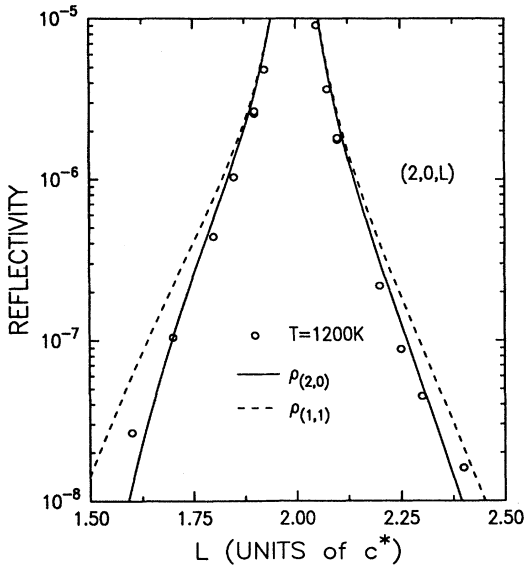

FIG. 18. Nonspecular x-ray reflectivity along the $(2,0,L)$ direction at $T=1200$ K. The dashed line is the reflectivity calculated assuming $\rho_{(2,0)}(n)=\rho_{(1,1)}(n)$. The solid line is a fit to the data as described in the text.

VI. CONCLUSION

In conjunction with the in-plane measurements described in Ref. 1, we have carried out detailed, absolute measurements of the specular and nonspecular reflectivities from the Au(001) surface. Below $T=1170$ K, the surface is well described by a corrugated, incommensurate hexagonal overlayer. The corrugation propagates several layers into the bulk. The effect of the distortion on the reflectivity appears to be the same at $T=300$ as at 1100 K even though the surface undergoes a first order rotational transition at $T=970$ K. We have also observed an increase with temperature of the thermal vibrational amplitudes for several near-surface layers. Above $T=1170$ K the hexagonal rods disappear and the Q_z dependence of the $(1,1,L)$ and $(2,0,L)$ rods is consistent with a disordered surface extending over several atomic layers. Although the effective surface-normal displacement amplitudes are large, atoms still reside in well-defined layers.

ACKNOWLEDGMENTS

We are grateful to G. Ownby for technical assistance. We thank D. Abernathy, G. Grübel, I. K. Robinson, A. Sandy, and Jia Wang for useful discussions. Work at Brookhaven was supported by the U.S. Department of Energy under Contract No. DE-AC02-76CH00016. Work at MIT was supported by the U.S. National Sci-

ence Foundation under Grants No. DMR-8806591 and No. DMR-8719217. Work at ORNL was sponsored by the Division of Materials Sciences, U.S. DOE under contract No. DE-AC02-84OR21400, with Martin Marietta Energy Systems Inc. X20 is supported by the NSF MRL Program at MIT (Grant No. DMR 8719217) and by IBM. CHESS is supported by NSF Grant No. DMR 8719764.

[1]D. Gibbs, B. M. Ocko, D. M. Zehner, and S. G. J. Mochrie, Phys. Rev. B **42**, 7330 (1990).
[2]B. M. Ocko and S. G. J. Mochrie, Phys. Rev. B **38**, 7378 (1988).
[3]D. Gibbs, B. M. Ocko, D. M. Zehner, and S. G. J. Mochrie, Phys. Rev. B **38**, 7303 (1988).
[4]I. K. Robinson, W. K. Waskiewicz, R. Tung, and J. Bohr, Phys. Rev. Lett. **57**, 2714 (1986).
[5]J. W. M. Frencken and J. F. van der Veen, Phys. Rev. Lett. **54**, 134 (1985).
[6]J. W. M. Frencken, P. M. J. Maree, and J. F. van der Veen, Phys. Rev. B **34**, 7506 (1986).
[7]R. Lipowsky, U. Breuer, K. C. Prince, and H. P. Bonzel, Phys. Rev. Lett. **62**, 913 (1989).
[8]H. Löwen, T. Beier, and H. Wagner, Europhys. Lett. **9**, 701 (1989); Phys. B **79**, 109 (1990).
[9]P. H. Fuoss, L. J. Norton, and S. Brennan, Phys. Rev. Lett. **60**, 2046 (1988).
[10]F. Grey, R. Feidenhans'l, J. S. Petersen, M. Nielsen, and R. L. Johnson (unpublished).
[11]S. Dietrich and H. Wagner, Z. Phys. B **56**, 207 (1984).
[12]H. Dosch, L. Mailander, A. Lied, J. Peisl, F. Grey, R. L. Johnson, and S. Krummacher, Phys. Rev. Lett. **60**, 2382 (1988).
[13]S. G. J. Mochrie, D. M. Zehner, B. M. Ocko, and D. Gibbs, Phys. Rev. Lett. **64**, 2925 (1990).
[14]S. Alexander and J. P. McTague, Phys. Rev. Lett. **41**, 702 (1978).
[15]L. Grubuek and J. Bohr (unpublished).
[16]R. Lipowsky, Phys. Rev. Lett. **49**, 1575 (1983).
[17]R. Lipowsky and W. Speth, Phys. Rev. B **28**, 3983 (1982).
[18]Beautiful experiments on the layer-by-layer freezing of Sm-*A* liquid-crystal films are described by B. D. Swanson, H. Stragier, D. J. Sweet, and L. B. Sorenson, Phys. Rev. Lett. **62**, 909 (1989); and Ocko, *ibid.* **64**, 2160 (1990).
[19]B. Pluis, T. N. Taylor, D. Frenkel, and J. F. van der Veen, Phys. Rev. B **40**, 1353 (1989).
[20]For an exhaustive review of wetting, see S. Dietrich, in *Phase Transitions and Critical Phenomena,* edited by C. Domb and J. Liebowitz (Academic, London, 1986), Vol. 2.
[21]J. Q. Broughton and G. H. Gilmer, J. Chem. Phys. **79**, 5119 (1983).
[22]W. Schommers, Phys. Rev. B **32**, 6845 (1985).
[23]P. Carnevali, F. Ercolessi, and E. Tosatti, Phys. Rev. B **36**, 6701 (1987).
[24]P. Stoltze, J. K. Nørskov, and U. Landeman, Phys. Rev. Lett. **61**, 440 (1988); and unpublished.
[25]V. Heine and L. D. Marks, Surf. Sci. **165**, 65 (1986).
[26]P. Carnevali, F. Ercolessi, and E. Tosatti, Surf. Sci. **189/190**, 645 (1987).
[27]K. G. Huang, D. Gibbs, D. M. Zehner, A. R. Sandy, and S.G.J. Mochrie, Phys. Rev. Lett. **65**, 3313 (1990); A. R. Sandy, S.G.J. Mochrie, D. M. Zehner, K. G. Huang, and D. Gibbs, Phys. Rev. B **43**, 4667 (1991).
[28]B. Pluis, A. W. Denier van der Gon, J.W.M. Frencken, and J. F. van der Veen, Phys. Rev. Lett. **59**, 2679 (1987).
[29]K. C. Prince, U. Breuer, and H. P. Bonzel, Phys. Rev. Lett. **60**, 1146 (1988).
[30]D. Beaglehole and D. Nason, Surf. Sci. **96**, 357 (1980).
[31]D. Zhu and J. G. Dash, Phys. Rev. Lett. **57**, 2959 (1986).
[32]R. R. Pandit and M. E. Fisher, Phys. Rev. Lett. **51**, 1772 (1983).
[33]S. G. J. Mochrie, M. Sutton, R. J. Birgeneau, D. E. Moncton, and P. M. Horn, Phys. Rev. B **30**, 263 (1984).
[34]F. Ercolessi, E. Tosatti, and M. Parrinello, Phys. Rev. Lett. **57**, 719 (1986).
[35]W. R. Busing and H. A. Levy, Acta Crystallogr. **22**, 454 (1967).
[36]S. G. J. Mochrie, J. Appl. Cryst. **21**, 1 (1988).
[37]A. Braslau, P. S. Pershan, G. Swislow, B. M. Ocko, and J. Als Nielsen, Phys. Rev. A **38**, 2457 (1988).
[38]S. P. Withrow, T. H. Barret, and R. J. Culbertson, Surf. Sci. **161**, 584 (1985).
[39]K. H. Rieder, T. Engel, R. H. Swendsen, and M. Manninen, Surf. Sci. **127**, 223 (1983).
[40]J. D. Axe, Phys. Rev. B **21**, 4181 (1980).
[41]B. M. Ocko, Jia Wang, Alison Davenport, and Hugh Isaacs, Phys. Rev. Lett. **65**, 1466 (1990).